Heat Transfer near an Isolated Hemispherical Gas Bubble: The Combined Influence of Thermocapillarity and Buoyancy

Séamus Michael O'Shaughnessy, Anthony James Robinson

Department of Mechanical & Manufacturing Engineering, University of Dublin, Trinity College, Ireland

Abstract

Thermal Marangoni convection about a 1 mm radius hemispherical air bubble attached to a heated wall immersed in a silicone oil layer of constant depth of 5 mm was numerically investigated. Tests were performed for a range of Marangoni numbers ($145 \leq Ma \leq 915$) with varying levels of gravitational acceleration between zero gravity and earth gravity in order to quantify the rates of heat transfer. For the zero gravity condition, a thermocapillary-driven vortex develops around the bubble extending the entire height of the channel. This flow structure causes a jet-like flow of heated liquid to emanate from the bubble tip which impinged on the cold wall. With the addition of gravity, a counter rotating secondary buoyancy-driven vortex forms which reduces the size of the thermocapillary vortex and disrupts the jet flow from the bubble tip. The wall heat flux profiles indicate that under zero gravity, the peak heat fluxes increase monotonically with *Ma* with an area of influence that increases asymptotically with *Ma*. Likewise, under gravity conditions the peak heat flux also increases with *Ma* and for low *Ma* is higher than that of 0-*g*. However, the area of influence is considerably smaller and not sensitive to *Ma* or the level of gravity. Experimental validation of selected terrestrial gravity numerical results was obtained using particle image velocimetry (PIV) for low to moderate Marangoni numbers. For all experiments, steady-state Marangoni convection was observed. The experimental flow patterns showed good agreement with the numerical solutions.

Keywords

Marangoni, thermocapillary, heat transfer, bubble, gravity, experimental, numerical

1. Introduction

Thermal Marangoni convection can occur when a gas-liquid interface has a non-uniform temperature distribution. The surface tension variation with temperature induces a stress imbalance which is equalized by causing local fluid motion and subsequent sheer stress. For the situation of a bubble attached to a heated wall, thermocapillary convection can cause notable enhancement of the wall heat transfer both in microgravity [1, 2] and at terrestrial gravity [3-5].

The contribution of thermocapillary convection on the local heat transfer about bubbles situated on a heated surface is still unclear. Much of the past experimental research into bubble-induced thermal Marangoni convection has been concerned with analysis of the flow field and has not been specifically concerned with the heat transfer, such as studies in Ref. [6-10]. A typical experiment would be conducted at earth gravity and involve a test chamber with a working fluid enclosed between a heated upper surface and a cooled lower one [4, 6, 11, 12]. A bubble would be injected in such a way that it is situated on the heated wall and protrudes into the thermal gradient established by the hot and cold plates. Since most fluids have a negative coefficient of surface tension, this configuration establishes a surface tension gradient along the bubble interface which leads to a liquid flow in the direction of increasing surface tension. The resulting surface tension force is opposed by the shear stresses within both the gas and liquid phase which establishes mechanical equilibrium around the stationary bubble.

The tank tread-like motion of the interface draws cool liquid from the bulk across the hot surface and subsequently propels the liquid downward back into the bulk from the bubble tip. The fluid motion near the wall reduces the thermal boundary layer thickness and results in higher heat transfer rates compared with the far field [13].

One of the earliest postulations regarding Marangoni convection and its influence on surface heat transfer was made by Pike *et al.* [14]. Studying the influence of dissolved gas on surface boiling the results showed that dissolved gas caused the onset of surface boiling to move to a lower surface temperature than anticipated. This suggested that the heat transfer from the surface to the bulk liquid was enhanced and was hypothesized as being Marangoni convection [15].

Possibly the first study aimed to quantify the rates of heat transfer resulting from Marangoni convection around a bubble situated on a heated wall was performed by Larkin [16]. Larkin numerically simulated the coupled flow and heat transfer problem in a semi-infinite fluid for a hemispherical bubble situated on an upward facing heated wall. The local Nusselt number distribution along the wall around the bubble was estimated and heat transfer enhancement levels of 30% over that of the far field were found for very high Marangoni numbers ($Ma \sim 10^5$). It was concluded that, based on the simulation results, Marangoni convection is an important heat transfer mechanism only at high Ma.

Soon afterwards, Kenning and Kao [17] reported a limited set of heat flux estimations from their numerical study of Marangoni flow around downward facing bubbles. With regard to the heat transfer rates they concluded that the heat transfer enhancement was confined to a small region along the wall and, for their zero gravity simulations, was dependant on the Marangoni Number.

In his review paper, Straub [3] reported thermocapillary augmented heat transfer around bubbles from both experimental and numerical studies. With regard to bubbles attached to heated surfaces, the results showed notable heat transfer enhancement and, for zero gravity, oscillatory behaviour at high Marangoni numbers ($Ma>2.5x10^5$). Following on from earlier work [3, 18, 19] Betz and Straub [11] numerically investigated the flow and heat transfer around bubbles attached to a heated wall in a cavity. The influence of the Marangoni, Prandtl, Peclet and Bond numbers were investigated. They determined that thermocapillary convection was strong enough to drive liquid flow against the action of buoyancy at earth gravity and thus have a notable influence on the heat and mass transfer around the bubbles. The influence of the Prandtl number was found to be negligible in the range $7\leq Pr\leq 120$ and the heat transfer was found to improve with reducing magnitude of the gravitational field strength. For large downward facing bubbles an empirical correlation was proposed for the Nusselt number of the form $Nu=1+fMa^{0.333}$. The multiplier f depended on the bubble volume and the height of the liquid layer.

Bhunia & Kamotani [REF] numerically investigated 2D flow around a bubble under a heated wall in a channel filled with a cross-flowing silicone oil (Pr = 70) under microgravity conditions. It was determined that for zero channel flow velocity, thermocapillary convection occurred as symmetric vortices about the vertical bubble axis. The introduction of a channel flow velocity caused a stagnation point to form on the bubble surface. For both zero and finite flow velocity, it was found that increasing the temperature difference strengthened the thermocapillary flow.

Arlabosse *et al.* [4] performed experiments using PIV for flow visualisation and interferometry for examining the temperature field around a downward facing bubble on a heated surface in a silicone oil layer. The influence of the temperature gradient, oil viscosity and bubble shape was analysed. Contrary to the experimental observation in [20], thermocapillarity was seen to be active along the entire contour of the bubble and was dominant over the buoyancy-driven convection in the immediate vicinity of the bubble surface. Weak secondary counter-rotating vortices beneath the primary vortices were observed due to the interaction of surface tension and gravity forces. The velocity of the liquid along the interface was measured to increase with increasing Marangoni number, but the location of the maximum velocity was independent of the Marangoni number. Heat transfer measurements were recorded using heat flux sensors located on the cold wall beneath the bubble. For a 3mm layer depth, they developed an empirical correlation for the heat transfer which was posed as;

$$\frac{q''_{Ma}}{q''_{cond}}=1+0.00841Ma^{0.5} \tag{1}$$

The efficacy of this correlation on the lower cold wall heat transfer enhancement was later confirmed by the numerical investigation of O'Shaughnessy and Robinson [13]. Before this, however, Petrovic *et al.* [5] used the same correlation to predict the heat transfer rate from an upward facing surface with several gas bubbles attached to it. In these experiments, a Marangoni-dominated heat transfer regime was discovered to exist between natural convection and subcooled nucleate boiling. Gas bubbles spontaneously formed on the surface due to dissolved air in the working fluid, which was water. The appearance of the bubbles resulted in a drastic enhancement of the surface averaged heat transfer coefficient over both natural convection and subcooled boiling. The authors used photographic information regarding the size and number of bubbles on the surface together with Eq. 1 to estimate the contribution of Marangoni convection to the overall surface heat flux. Although the model predicted the Marangoni heat flux adequately, it required assumptions with regard to the heat transfer coefficient and area of influence of Marangoni heat transfer for each bubble.

O'Shaughnessy and Robinson [13, 21, 22] were the first to numerically simulate thermal Marangoni convection with the expressed goal of quantifying the local wall heat transfer distribution around the bubbles. In [13] they investigated the influence of increasing the Marangoni number in 0-g and determined that thermocapillary convection enhanced the local heat flux to over 65% when compared with pure conduction. Enhancment of local wall heat transfer was calculated to occur over a distance of approximately seven bubble radii. The numerical results indicated that the ratio of Marangoni heat transfer to conduction over the area of enhancement changes approximately with the square root of the Marangoni number according to

$$\frac{q''_{Ma}}{q''_{cond}}=1+0.005Ma^{0.5} \tag{2}$$

In [22], O'Shaughnessy and Robinson investigated the influence of the Rayleigh number for a fixed Marangoni number and found that the gravity level affected the velocity profile by modifying the interfacial temperature gradient, but that the location of maximum velocity was almost independent of gravity level. It was also shown that increased gravity levels cause a reduction in the effective radius and area of enhancement around the gas bubble.

In this work the overarching objective is to contribute to knowledge regarding Marangoni convection and heat transfer around isolated bubbles. The specific objectives are as follows:

1. To provide a limited set of experimental flow visualization results for a simple geometric configuration for validating numerical simulations.

2. To develop a correct mathematical model for thermal Marangoni convection around a bubble and numerically simulate the phenomena using a commercial CFD software package.

3. To investigate the flow and heat transfer in the vicinity of the bubble for varying levels of gravitational and thermocapillary influence and attempt to disentangle their influence on the flow and heat transfer.

4. To provide some simple-to-use guidelines for predicting the average heat transfer coefficient around bubbles on downward facing surfaces.

2. Numerical Procedure

For Marangoni convection around a bubble of radius R_b within a channel of height H, the mass and heat transport mechanisms are characterised by the Prandtl, Rayleigh, Marangoni and Bond numbers, defined respectively as [4, 23-25],

$$Pr = \frac{\upsilon}{\alpha} \tag{3}$$

$$Ra = \frac{g\rho\beta\Delta T R_b^4}{\mu\alpha H} \tag{4}$$

$$Ma = -\left(\frac{d\sigma}{dT}\right) \times \frac{\Delta T}{\mu\alpha} \times \frac{R_b^2}{H} \tag{5}$$

$$Bo = -\frac{\rho g\beta R_b^2}{(d\sigma/dT)} \tag{6}$$

The commercial code Fluent version 6.3.26 was utilized to solve the system of governing equations. Simulations were performed to investigate the influence of both the thermocapillary driving potential (*Ma*) and the buoyancy driving potential (*Ra*) on the flow and temperature fields as well as local heat transfer profiles. A numerical model for the domain depicted in Figure 1 was constructed using Gambit version 2.2.30. The numerical mesh consisted of approximately 8x10^4 cells. The calculation of surface tension effects in Fluent is more accurate on quadrilateral cells and grid clustering was used in the vicinity of the interface. Grid independence was achieved by increasing the number of mesh cells and observing the convergence of certain local parameters of interest such as free surface velocity and temperature, wall heat flux, and also by tracking global parameters such as total rate of heat transfer and conservation of mass through the system.

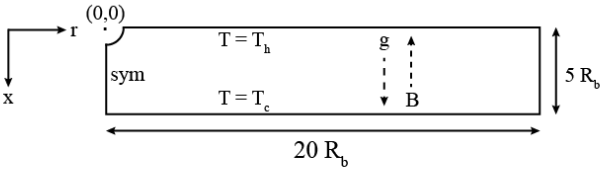

Figure 1: Numerical domain

The numerical model assumes steady state for an incompressible fluid with constant fluid properties and an adiabatic, non-deformable hemispherical bubble interface.

The assumption that no heat transfer occurs across the bubble interface means that the work presented in this study is not directly applicable to nucleate pool boiling, during which evaporation at the interface acts to suppress the thermocapillary flow. The assumption is consistent with the Marangoni heat transfer regime discovered by Petrovic et al. [5] where air bubbles caused a noteworthy enhancement in the wall heat transfer even when the heated wall temperature was below the saturation temperature. The work is also qualitatively comparable to the situation of gas-saturated liquids, for example, the experimental results of Henry et al. [26].

To non-dimensionalize the governing equations it was necessary to select several reference scales. Consistent with the work of Arlabosse *et al.* [4], the following reference parameters were chosen:

Table 1: Reference parameters

length	L_{ref}	R_b
temperature	T_{ref}	$(T_h - T_c)\left(\frac{R_b}{H}\right)$
velocity	v_{ref}	$\frac{(d\sigma/dT)(T_h - T_c)R_b}{\mu H}$
pressure	p_{ref}	ρv_{ref}^2
time	t_{ref}	$\frac{L_{ref}}{v_{ref}}$

The governing equations of continuity, momentum and energy can then be expressed in dimensionless form (the prime symbol denotes a dimensionless quantity):

$$\nabla' \cdot \boldsymbol{v}' = 0 \tag{7}$$

$$(\boldsymbol{v}' \cdot \nabla')\boldsymbol{v}' = -\nabla' p' + \frac{Pr}{Ma}\nabla'^2 v' + \sum F' \tag{8}$$

$$\nabla' \cdot (\boldsymbol{v}'\theta') = \frac{1}{Ma}\nabla'^2\theta' \tag{9}$$

In the above equations, $\Sigma F'$ represents the sum of all dimensionless body forces acting on the fluid. This term includes the buoyancy forces due to the presence of a gravitational field, which is modelled using the Boussinesq approximation. Consistent with the continuum surface force (CSF) model employed by Fluent, the effects of surface tension are also included as a source term in the momentum equation. Details of the CSF model can be found in Brackbill *et al.* [27]. For this study,

$$\sum F' = -\frac{BoPr}{Ma}\theta' + \frac{Pr}{Ma}\left(\frac{d\sigma}{dT}\right)'\frac{d\theta'}{ds'}\kappa' \qquad (10)$$

The numerical domain places a bubble of dimensionless radius of unity at the centre of an axisymmetric domain of five bubble radii height and outer radius of twenty bubble radii (Fig. 1). This length was chosen so that the influence of the side walls would be negligible. The vertical axis denoted ‘sym’ signifies the axis of symmetry. The upper wall, to which the bubble is attached is no-slip, constant temperature, and is maintained at the dimensionless temperature H/R_b for all simulations. This wall is termed the ‘hot’ wall hereafter. The lower horizontal wall is also no-slip, constant temperature and the temperature of this wall is maintained at the dimensionless temperature of zero for all simulations, and is termed the ‘cold’ wall henceforward. The vertical wall placed twenty bubble radii from the centre of the bubble has no-slip, adiabatic boundary conditions. The bubble interface is adiabatic and non-deformable. The velocity boundary condition along the bubble interface is derived from the CSF model.

$$\boldsymbol{v} = 0|_{x'=5} \qquad \theta' = 0|_{x'=5} \qquad (11)$$

$$\boldsymbol{v} = 0|_{x'=0} \qquad \theta' = (H/R_b)|_{x'=0} \qquad (12)$$

$$\boldsymbol{v} = 0|_{r'=20} \qquad \boldsymbol{n}\cdot(\nabla'\theta') = 0|_{r'=20} \qquad (13)$$

Simulations were performed for Marangoni numbers in the range $145 \leq Ma \leq 915$ and dimensionless gravity levels of g' = 0, 0.01, 0.1, 0.25, 0.5, 0.75 and 1, where the term g' corresponds to the dimensionless gravity level g/g_{earth}.

3. Experimental Setup

Experiments were performed to analyse Marangoni flow about a 1mm radius bubble on a heated wall in a Pr = 220 liquid silicone oil layer of depth H = 5mm under terrestrial conditions. The fluid properties of the silicone oil used in the experiments (and in the evaluation of the dimensionless numbers) as obtained from the manufacturer are provided in Table 2. PIV data was obtained for horizontal wall temperature differences ($T_h - T_c$) of 20°C, 30°C, 40°C and 50°C, which correspond to Marangoni numbers of Ma = 145, 218, 290 and 363 respectively.

Table 2: Properties of Dow Corning® silicone oil 20cSt at 25°C, 1atm

ρ	950	[kg/m^3]
υ	20e-6	[m^2/s]
k	0.14	[W/mK]
C_p	1630	[J/kgK]
β	1.07e-3	[1/K]
$d\sigma/dT$	-6.23e-5	[N/mK]

The test section consists of two copper surfaces, one heated to a constant temperature which is varied between experiments, and one cooled to a constant and lower temperature. Both interior copper surfaces are coated with a thin layer of matt black paint to minimise reflections from laser light. The copper surfaces are housed in a Perspex container which dictates the test cell height to 5mm. A sketch of the test section and flow loop is provided in Figure 2.

The upper wall is maintained at the elevated temperature by a sealed 30mm x 30mm Peltier element (Melcor, CP1.0-127-05L-RTV), capable of delivering a maximum power of around 40W. The temperature of the wall is measured using a calibrated K-Type thermocouple placed close to the bubble injection site. Once steady state is achieved, the temperature of this wall can be maintained to within +/- 0.2°C of the desired temperature setpoint.

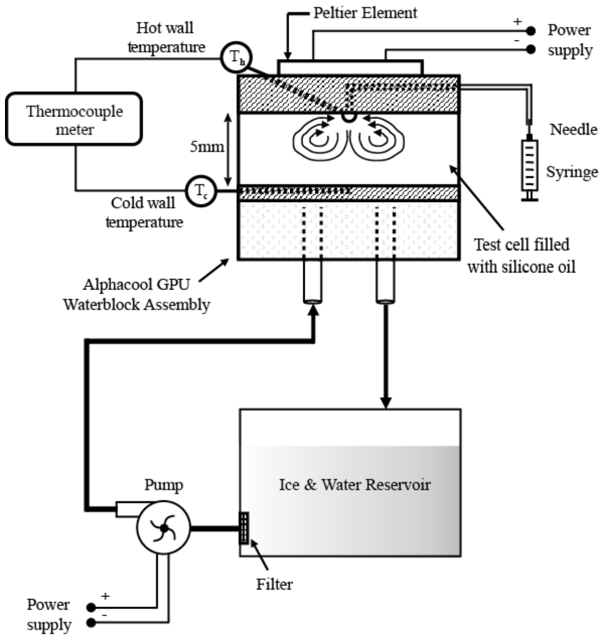

Figure 2: Experimental flow loop

The cold wall temperature is maintained by a water flow loop. An ice bath ensured a constant water temperature. An off-the-shelf liquid cooled graphics card heat sink (Alphacool Videocard NexXxos GP1X-N Geforce VGA Waterblock) is utilised as the cold side of the test chamber. The exposed copper surface of the heat sink is smooth and polished. The heat sink base is mounted on the Plexiglas housing with an O-ring to prevent leakage. Both the copper and Plexiglas are connected via four screws. A stainless steel mounting plate of 1mm thickness is located around the perimeter of the underside of the copper section. The Plexiglas housing is connected to 12.7mm internal diameter tubing via two compression fittings. The tubing runs to and from a water reservoir filled with crushed ice. The cooled water is pumped through the tubing to the copper waterblock, lowering the wall temperature close to 0°C. Since phase change is an isothermal process, the iced-water reservoir delivers a reliable, constant temperature cold source. A calibrated K-Type thermocouple is placed in the lower wall very close to the surface to monitor the cold wall temperature. Typically, the cold wall temperature can be maintained at 0.2°C +/- 0.2°C.

Bubble injection onto the hot wall is achieved via an infusion pump fitted with a syringe, which is connected to a 0.8mm internal diameter flexible piece of Tygon® tubing. The tubing is placed within the upper wall and connects with an orifice located on the underside of the heated wall. The volume of the bubble is controlled with adequate accuracy by the infusion pump. A single bubble of approximate radius R_b=1mm is injected for each experiment in this study. Two holes are drilled in the upper copper section far from the bubble orifice to allow for expansion of the liquid due to heating and bubble injection. The test cell is overfilled gradually with the seeded silicone oil through the expansion holes using the syringe and infusion pump. This ensures that the trapped air in the test cell is removed.

Flow visualization was achieved using a Quantronix Darwin Duo high repetition Nd:YLF laser (neodymium: yttrium lithium fluoride, λ = 527 nm, 0.1-0.3 J/s at 1000 Hz) in combination with a high speed CMOS Photron camera. PIV recordings in this investigation were obtained using the software package DaVis version 7.2. A sketch of the PIV setup is provided in Figure 3. The silicone oil is seeded with hollow glass spheres of mean diameter in the range of 9-13μm, and a density of 1100 +/- 50 kg/m^3. These seeding particles are recommended for oil and water flows [28], and have been used in similar studies [20]. Depending on the flow velocity and the factor of magnification of the camera lens, the delay of the laser pulses is chosen such that adequate displacement of the particle images on the CCD camera is obtained. An acceptable particle image shift is approximately 5 pixels. Since thermocapillary flows are generally quite slow, the camera was set to record in single-frame mode. Each image in the PIV recording is subdivided into interrogation windows. Each interrogation window produces a single vector after statistical correlation methods have been employed.

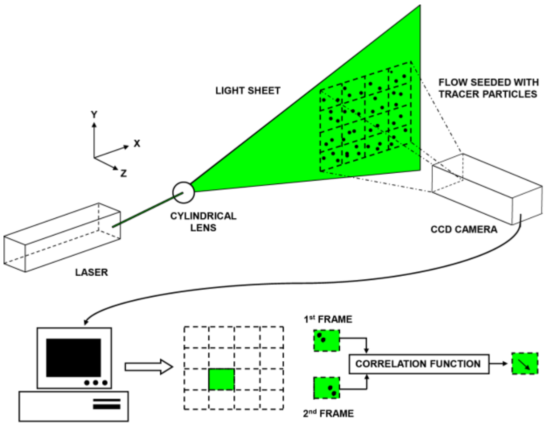

Figure 3: Particle image velocimetry

Once the vector fields are computed, the average vector field and the RMS deviation from the average are determined according to Eq. 15 and Eq. 16 respectively.

$$\boldsymbol{v_{avg}} = \left(\sum_{i=1}^{n} \boldsymbol{v_i}\right) \Big/ \boldsymbol{n} \tag{14}$$

$$\boldsymbol{v}_{rms} = \sqrt{\left(\sum_{i=1}^{n} \left(\boldsymbol{v}_i - \boldsymbol{v}_{avg}\right)^2\right) \Big/ (n-1)} \tag{15}$$

For fluid flows, the particle size is generally not as critical as in gas flows [28, 29]. One source of error is the influence of gravitational forces brought about by the difference in density between the test fluid and the tracer particles. The gravitationally induced velocity of a particle undergoing Stokes flow, $\boldsymbol{u}_g$, is given by Raffel [28]:

$$\boldsymbol{u}_g = d_p^2 \frac{(\rho_p - \rho_f)}{18\mu} \boldsymbol{g} \tag{16}$$

For this study, $\boldsymbol{u}_g$, ≈ 7x10^{-4}mm/s which was small relative to the maximum velocities expected in the thermocapillary induced flow. Furthermore, the particle Reynolds number is given by

$$Re_p = \frac{\rho_f(\boldsymbol{u_f} - \boldsymbol{u_p})d_p}{\mu_f} \tag{17}$$

The tracking capability of a tracer particle is also described by Melling [29] and Tchen [30]. Calculations of the Reynolds number produce a maximum $Re \approx$ 2.5x10^{-3}, so approximations of Stokes flow are justified. Integration of the force balance equation described by these authors using a nominal vertical velocity of 1mm/s and Stokes flow approximation for the drag force resulted in an average fluid velocity of 0.3173mm/s and an average particle velocity of 0.3160mm/s. Thus, while also considering the negligible effect of gravitational induced velocity, it may be assumed that the particles represent the flow quite accurately.

4. Validation of Numerical & Experimental Approach

To verify the correctness of both experimental procedure and the numerical approximation of axial symmetry, simulations were performed to replicate as closely as possible the experimental conditions. Figure 4 shows the numerical (coloured by stream function) and experimental streamlines for each of the Marangoni numbers tested. The simulated streamlines appear on the left of each figure. For clarity, a red line has been included in the experimental data on the right hand side of the figures to indicate the position of the gas bubble interface. The temperature differential and Marangoni number increase with successive images and the density of streamlines is kept constant for all images. By comparing the position, size and shape of the main and secondary vortices with the numerical solutions, good qualitative agreement is observed.

The temperature gradient existing along the bubble causes a surface tension gradient along the gas-liquid interface, inducing Marangoni convection. Fluid is entrained near the base of the bubble, dragged along the interface toward the bubble tip and leaves as a jet-like flow. This type of flow has been observed in several studies [4, 8, 10, 23-25, 31].

The streamline plots detail the presence of a toroidal main vortex adjacent to and wrapping around the bubble. This vortex is caused by the thermocapillary effect and acts to re-circulate cold fluid from the lower regions of the test cell toward the heated wall. These vortices have been observed experimentally by several authors [4, 7, 9, 20].

A secondary toroidal vortex can be seen beneath the primary vortex. The formation of the secondary vortex is discussed by Kassemi and Rashidnia [12]. The buoyancy force acts in opposition to the downwardly directed thermocapillary flow and the stabilizing density gradients exert a restoring upward force on the downward flowing hot liquid. This restricts the flow, compressing the primary vortex to the region of the hot wall and bubble. These opposing influences induce the counter-rotating shear-driven secondary vortex.

For the experiments conducted in this study, the secondary vortex moves more slowly than the primary vortices and attempts to re-establish the thermal stratification of the fluid by moving warmer fluid toward the heated wall. There is a stagnation point at the boundary between the primary and secondary vortices. Since the temperature gradient increases with successive images, it is evident that both the primary thermocapillary-driven and the secondary buoyancy-driven vortices increase in strength with increasing *Ma*.

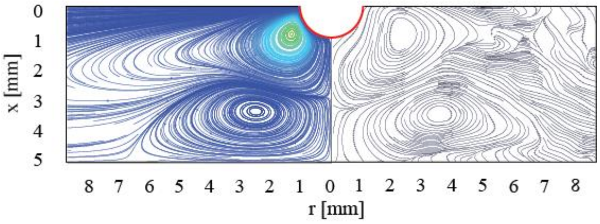

(a) *Ma* = 145

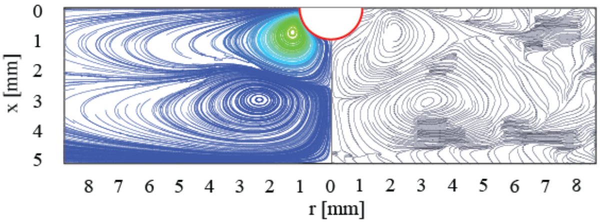

(b) *Ma* = 218

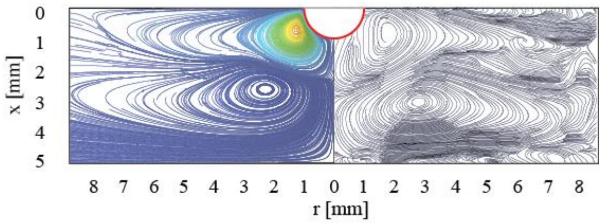

(c) *Ma* = 290

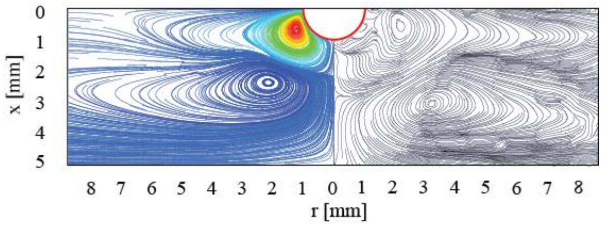

(d) *Ma* = 363

Figure 4: Numerical (left) and experimental (right) streamlines for $Pr = 220$ and $145 \leq Ma \leq 363$

In Figure 4-a, the primary thermocapillary vortex appears to be marginally larger than the secondary buoyancy induced vortex. The intensity of both vortices increases with increasing temperature gradient. Indeed, the fluid velocity increases with increasing *Ma*. However, with increasing *Ma* the primary vortex is squeezed and pushed closer towards the bubble cap, a phenomenon also observed by Raake *et al.* [20]. Interestingly, the stagnation points also move toward the bubble with increasing *Ma*, and an elongation of both vortices is observed. This may indicate that the buoyancy-driven vortex is gaining in intensity at a rate greater than that of the thermocapillary-driven vortex. Hence, further increases in the temperature gradient may result in the Marangoni flow being confined to a region in the immediate vicinity of the bubble until the flow structure becomes unstable, and an oscillatory mode occurs.

The comparison of the predicted fluid axial velocity with the experimentally measured data is shown in Figure 5. Data is measured from the bubble tip to the cold wall. Overall, agreement of the numerically predicted and experimentally measured peak velocities ranges between approximately 10% ~ 20% for the *Ma* range tested which is deemed acceptable.

For the experimental data the bubble tip is not as well defined since the reflection of laser light in the bubble can cause both high intensity light spots and local shading. For each temperature differential tested, the numerical and experimental curves follow the same trend. The axial velocity is zero at the bubble tip and then increases rapidly until a peak at approximately $x/R_b \sim 1.3$. This increase is caused by the jet-like flow of liquid away from the bubble tip. From this point there is a similarly sharp decrease in axial velocity as the Marangoni influence diminishes with increasing distance from the bubble and the fluid is pulled into the rotating primary vortex. The axial velocity is then observed to drop below zero. This sign change is significant as it highlights the crossover from the primary vortex to the secondary counter-rotating vortex, and hence the crossover from thermocapillary dominated flow to one driven by buoyancy. As the cold wall is approached, both the simulated and measured axial velocities tend towards zero. Clearly, for each Marangoni number tested, the measured axial velocity peak is greater for the thermocapillary vortex than that of the buoyancy vortex. With increasing *Ma* the crossover point occurs closer to the bubble as the secondary vortex squeezes the primary one.

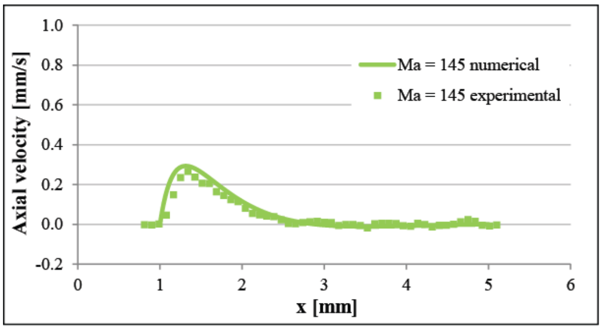

(a) *Ma* = 145

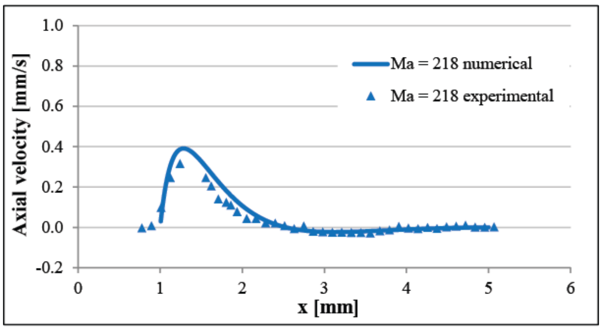

(b) *Ma* = 218

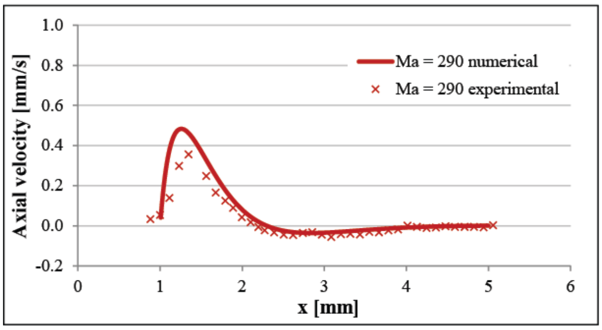

(c) *Ma* = 290

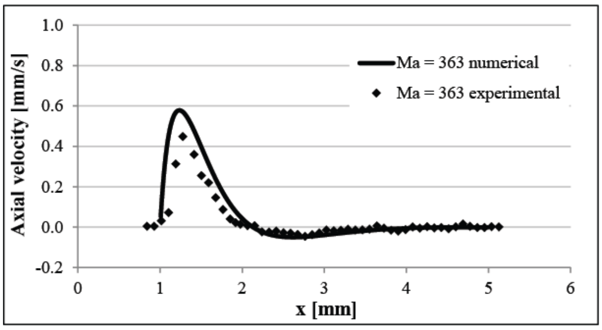

(d) *Ma* = 363

Figure 5: Numerical and experimental axial velocity plots for $Pr = 220$ and $145 \leq Ma \leq 363$

5. Results & discussion of numerical simulations

Further simulations were conducted to investigate the combined influence of the *Ma, Ra* and *Pr*.

5.1 Influence of *Ma*

Initial simulations were performed under zero gravity conditions in order to form a baseline understanding of the thermocapillary flow phenomenon for the configuration under test. Using a Pr = 220 fluid with fluid properties given by Table 2 previously, simulations were performed for Marangoni numbers in the range $145 \leq Ma \leq 363$. Figure 6 illustrates the temperature contours and streamlines for a range of Marangoni numbers under zero gravity conditions. The temperature and stream function scales are the same for all images. The effect of increasing Marangoni number under 0-*g* conditions has been investigated by O'Shaughnessy and Robinson [13]. Consistent with the findings in [13], thermocapillary convection causes the formation of a flow of liquid away from the bubble tip, which can be visualised by the way in which the temperature contours deflect away from the hot wall. This liquid then flows away from the centreline and forms a primary toroidal vortex around the bubble. The jet-like flow and primary vortex increase in velocity and intensity with increasing Marangoni number, but the size of the primary vortex does not change significantly. Indeed, to a large extent the channel height dictates the vortex size under zero gravity conditions [32-34]. Heat transfer is enhanced as the vortex recirculates colder fluid from the lower regions of the channel toward the hot wall.

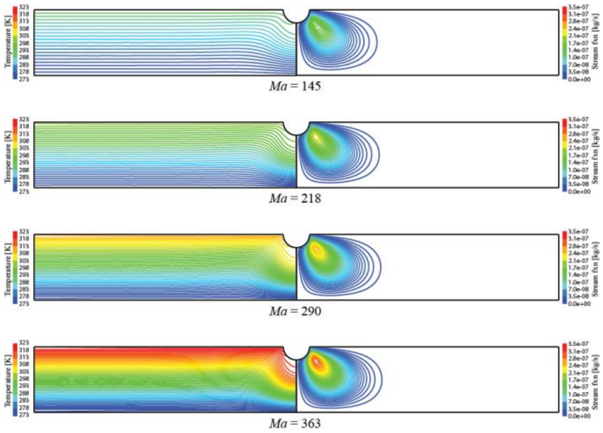

Figure 6: Temperature contours (left) and streamlines (right) for $145 \leq Ma \leq 363$ under zero gravity

When compared to pure conduction in the absence of the bubble, Marangoni convection augments the wall heat transfer over an area surrounding the bubble. The recirculating vortex draws cooled liquid from the cold wall towards the hot wall. Here the flow is redirected inward towards the bubble along the hot wall. The liquid convection reduces the thermal boundary layer thickness in this region which causes the local wall heat flux to increase over that of the far field.

The radial heat flux enhancement profiles are provided in Figure 7 for a range of Marangoni numbers. Clearly the region near the bubble experiences the largest improvement in wall heat flux, with higher Marangoni numbers producing greater enhancement since the intensity of the vortex increases. For these zero gravity simulations, all curves converge to the zero-enhancement line at approximately the same radial location, as observed in [13]. This location (r/R_b ~ 8) marks the point at which thermocapillary convection ceases to significantly affect the wall heat transfer. All curves converge at the same location because under zero gravity the thermocapillary driven vortex does not significantly change in size with changing *Ma*, as was shown in Figure 6.

Under zero gravity conditions, the cold wall opposite to the bubble also experiences large increases in the heat flux. The liquid which was heated at the opposite wall is propelled away from the bubble by the thermocapillary effect at the bubble interface. As the cold wall is approached the primarily axially directed jet flow is redirected laterally from the stagnation point forming a wall jet. The impinging jet results in a reduction in the thermal boundary layer thickness from the stagnation point outward, which is clearly evident in Figure 6. Here the liquid is cooled and drawn away from the cold wall towards the hot one in order to conserve mass since the domain is closed around the outer edge. This recirculation of the fluid forms the vortical structure and partially explains why its overall size is primarily determined by the chamber height. As with the hot wall, the level of enhancement on the cold wall increases with *Ma* although the area of influence does not. The radius of influence on the cold wall is much smaller (~4R_b) and now has a bell shaped profile typical of an impinging jet. Since the area of influence is much smaller, the increase in the peak heat fluxes are much larger compared with the hot wall, reaching nearly twofold at Ma = 363.

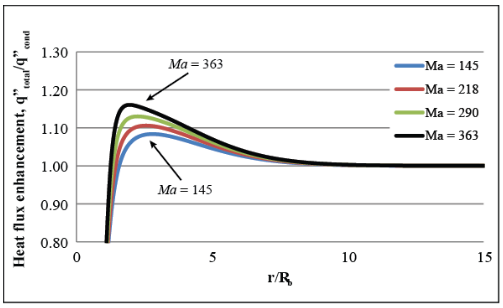

(a) Hot wall

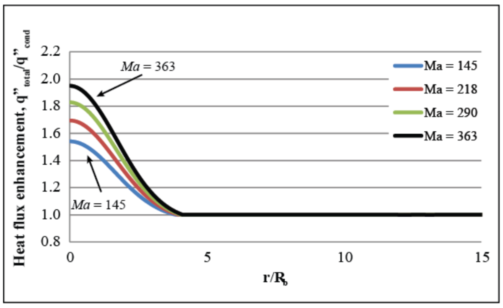

(b) Cold wall

Figure 7: Heat flux enhancement under zero gravity

5.2 Influence of *Ra*

The influence of the magnitude of gravitational acceleration on Marangoni convection about an isolated bubble on a heated wall has been numerically investigated in [22]. To study the response to changing gravitational field strength, simulations were initially performed for a range of gravity levels at a fixed Marangoni of *Ma* =363, which corresponded to the largest temperature gradient imposed on the channel experimentally (~50°C). The flow and temperature fields are detailed in Figure 8. Again, the same colour scale is applied to each plot.

Figure 8 highlights the formation of the secondary vortex, which is quite obviously due to the buoyancy effect since it does not occur under zero gravity condition. Simulations show that the secondary counter-rotating vortices develop within the flow structure from gravity levels as low as $g' = 0.1$. The addition of gravity induces the force of buoyancy which acts in opposition to the downwardly directed thermocapillary flow. The stabilizing density gradients exert a restoring upward force on the downward flowing hot fluid. This acts to restrict the flow causing the primary vortex to compress against the region of the heated top wall and bubble. The opposing influences provoke a counter-rotating shear-driven secondary vortex as depicted in Figure 8. This behaviour has been observed in [20, 22, 32].

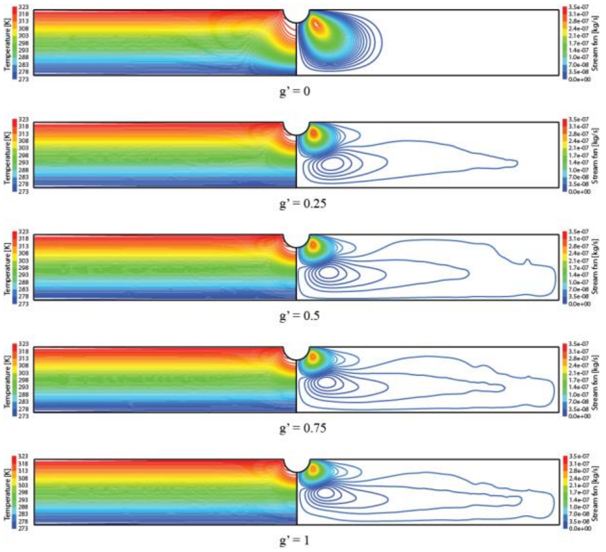

Figure 8: Temperature contours (left) and streamlines (right) at *Ma* = 363 for *g'* = 0, 0.25, 0.5, 0.75, and 1

From the figure it is evident that with increasing gravitational acceleration, and therefore increasing buoyancy effect, the thermocapillary effect becomes progressively more confined to a region close to the bubble. Once the secondary vortex appears the temperature contours which protrude from the hot wall and bubble apex at 0-*g'* are now restricted to a region closer to the interface. At 0-*g'* the thermal energy was transported to a localized region of the cold wall directly opposite to the bubble by the jet emanating from the bubble tip. For the higher gravity levels the heated liquid is initially propelled downward by the primary vortex and subsequently entrained into the secondary vortex which convects the heat laterally over a substantial portion of the lower section of the domain.

It is also noted that the primary thermocapillary-driven vortex shrinks with increasing gravity level. This behaviour is a result of natural convection attempting to restore the thermal stratification that would exist in the absence of the bubble. In particular, the jet-like flow stemming from the bubble apex becomes restricted by the buoyant forces opposing it.

The radial heat flux enhancement profiles are provided for *Ma* = 363 and a range of gravity levels in Figure 9a and Figure 9b for the hot and cold walls respectively. It is clear that gravity has a strong influence on the heat flux distribution profiles. Under zero gravity, the area influenced by Marangoni convection spread to a distance of up to 8 bubble radii on the 'hot' wall, but this value is more than halved at earth gravity. Interestingly, once the secondary vortex has formed, increasing gravity has a minor influence on the heat transfer at the hot wall. In accordance, the peak heat flux enhancement appears to be dictated by the secondary vortices, with only small increases with increasing gravity level. The secondary vortices also prevent much of the warm fluid from reaching the cold wall, and thus the cold wall experiences little local heat flux increases under gravity, as evident from Figure 9b.

To investigate if this behaviour was consistent for all Marangoni numbers simulated, the radial heat flux profiles for the *Ma* = 145 case are presented in Figure 10. It is first noted that the heat flux at the cold wall is close to zero for all cases once the buoyancy driven vortex is established. Similarly, and regardless of *Ma*, once a buoyancy driven vortex is established the wall heat flux profiles are not hugely sensitive to the gravity level. Clearly, the area influenced by thermocapillarity decreases with increasing gravity level. Expectedly, the peak heat fluxes for the *Ma* = 145 case are lower than for the *Ma* = 363 case. However, these heat flux profiles show a somewhat different response to increasing gravity levels: the relative magnitude of the heat flux is shown to depend strongly on *Ma*.

For the *Ma* = 363 case the peak heat flux is much lower for the 0-g case while the radius of influence trends are similar to the lower *Ma* case. For *Ma* = 145 the peak heat flux for the 0-g case is closer to the value obtained for the 1-g case. Indeed, it would appear that once gravity is present and significant and the secondary vortex is formed, the hot wall heat transfer increases to a higher peak value and then drops off more rapidly compared with 0-*g*. In this way there are offsetting effects whereby the reduced area of influence caused by the smaller vortex is partially offset by a higher peak heat flux.

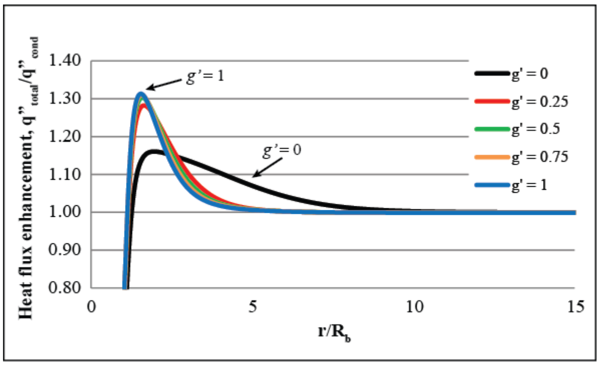

(a) Hot wall

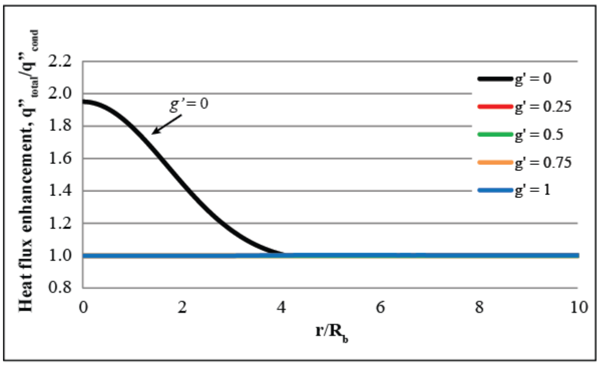

(b) Cold wall

Figure 9: Wall heat flux profiles for varying gravity simulations at *Ma* = 363

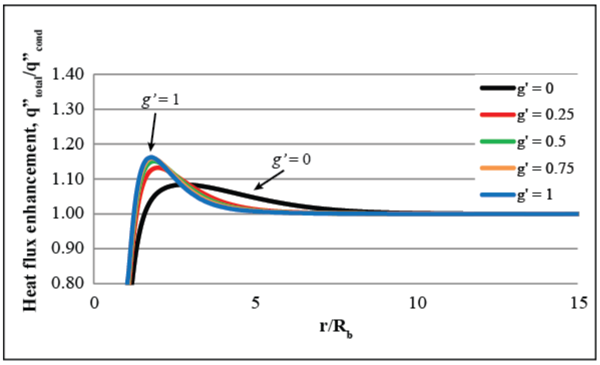

(a) Hot wall

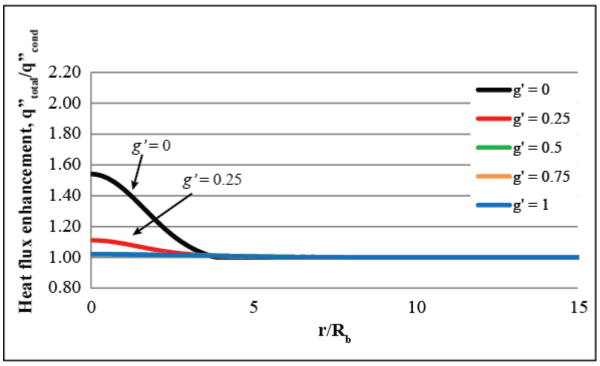

(b) Cold wall

Figure 10: Wall heat flux profiles for varying gravity simulations at *Ma* = 145

5.3 Combined Influence of *Pr*, *Ra* & *Ma*

In [23] it was concluded that the Rayleigh number modifies the flow pattern but has little influence on the strength of the primary vortex induced by the bubble. Contrastingly, it was found that the Marangoni and Prandtl numbers induced little change in the flow pattern but they respectively enhanced and reduced the strength of the primary thermocapillary vortex.

In [13, 22], simulations were performed using a *Pr* = 83 fluid and Marangoni numbers in the range 183≤*Ma*≤915. Using the same computational grid, the simulations performed in this study concern a *Pr* = 220 fluid in the range 145≤*Ma*≤363. Figure 11 plots both sets of non-dimensional results for the peak hot wall heat flux enhancement. Clearly, for all gravity levels simulated, the trends are similar irrespective of the Prandtl number.

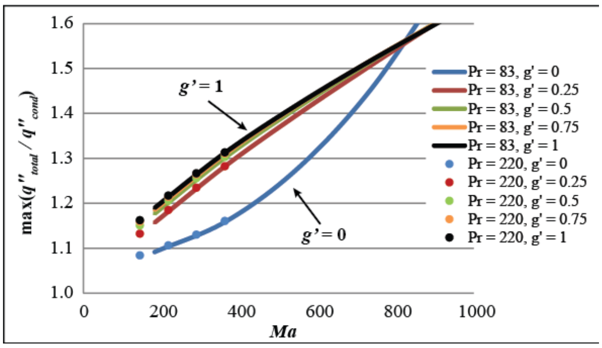

Figure 11: Influence of Prandtl number and gravity level on the peak hot wall heat flux enhancement

For gravity levels above 0.1-g the influence of gravity is small and there are two toroidal vortices. There is a transition, however, as gravity is reduced whereby the buoyancy influence disappears and the flow system becomes a single thermocapillary vortex that occupies the entire channel height. For these low gravity scenarios (<0.1-g) the heat flux profile is quite different to that of the higher gravity cases. Compared with the almost linear increase in the peak hot wall heat flux ratio for higher gravity, this ratio for the zero gravity case is parabolic to the extent that the peak heat flux is lower at low *Ma* though increases at a higher rate and is larger above *Ma* = 800.

In an effort to further elucidate the role of gravity in particular, the relative influences of thermocapillary and gravitational forces are to be analysed more closely. As the gravity level is increased beyond the magnitude required for the occurrence of secondary vortices the region where the vortices interact, i.e. the saddle point, is not affected greatly. The flow pattern has already been established, and buoyancy squeezes the primary vortex. Gravity, in the range tested, acts as a physical barrier for the thermocapillary flow, ostensibly confining it to the vicinity of the bubble as opposed to the channel. Gravity separates the flow, even at gravity levels as low as 0.1-*g*, as the flow structure is already established at this point. Once the buoyancy and thermocapillary zones are established, it is not expected that increasing the magnitude of gravitational acceleration will affect the flow structure in the thermocapillary-dominated zone significantly. This can be examined by considering a scaling argument applicable to the region near the bubble. In this region, thermocapillary induced inertia effects compete against gravity induced buoyancy effects. Scaling the inertial stresses with the buoyancy stresses in the momentum equation gives

$$\rho(\boldsymbol{v} \cdot \nabla)\boldsymbol{v} \approx \rho g \beta \Delta T \tag{18}$$

This, upon non-dimensionalizing with the appropriately chosen scales gives

$$\frac{\rho v_{ref}^2}{L_{ref}} \approx \rho g \beta \Delta T \tag{19}$$

which can be shown to be equivalent to

$$\frac{Ma^2}{RaPr} \approx 1 \tag{20}$$

This dimensionless ratio represents the relative magnitude of thermocapillary driven inertial forces to that of buoyancy and is equivalent to the inverse of the Richardson number in mixed forced and natural convective flows. This scaling argument would indicate that for gravity to have major influence in the region near the bubble, $Ma^2/RaPr$ must be in the order of unity. For the scenarios simulated in Figure 9 and Figure 10 the values of $Ma^2/RaPr$ corresponding with 0.25-*g* are 16.4 and 41 for the *Ma* = 145 & 363 cases respectively. These decrease to 4.1 and 10.2 for the 1-g cases. Since $Ma^2/RaPr > 1$ for these cases it is not surprising that gravity has little influence on flow structure and the measured wall heat transfer in the vicinity of the bubble.

Hence, to explain why the peak heat flux is lower for the 0-*g* case for low *Ma* and higher for high *Ma*, one must scrutinise the flow and temperature fields more closely. For each Marangoni number simulated, the interfacial fluid velocities are similar across the range of gravity levels, but the peak heat flux profiles can be very different. It appears as though this behaviour is due to the secondary vortex. Figure 12 plots the fluid pathlines coloured by velocity magnitude. A log scale is used so small changes in colour may represent a disproportionate change in velocity magnitude. The number of fluid pathlines displayed has also been reduced for clarity. It is noted that the range of Marangoni number investigated in this section is expanded up to *Ma* = 915 to highlight the influence of the secondary vortices.

If gravity is present and significant (≥0.1-*g*) and the Marangoni number is increased, both the thermocapillary and buoyancy forces increase in strength. The interfacial fluid velocity increases, but the secondary vortex prevents the thermocapillary vortex from spreading to the lower part of the domain. Indeed the secondary vortex may strip some of the kinetic energy from the thermocapillary roll. As the Marangoni number is increased, more energy appears to be transferred between the two vortices. The region where the two vortices come into contact is of special interest. As the Marangoni number is increased from left to right in the grid, one can see that the secondary vortex is growing in intensity at a rate higher than that of the primary vortex. The interfacial temperature gradients remain almost the same for all gravity levels, so the thermocapillary roll must be losing some of its mechanical energy to the secondary vortex.

For the *Ma* = 183 case in Figure 12, the introduction of gravity forms the secondary vortex which essentially deflects the primary vortex and confines it to the region near the bubble. The secondary vortex, which is driven by the primary one, is weak at low *Ma* so that in the context of the partitioning of kinetic energy from the source (i.e. the bubble interface), a large enough portion is still retained in the thermocapillary vortex causing its intensity to increase since it is now smaller. This causes the heat transfer to improve when the gravity influence takes hold. For the *Ma* = 915 case the same is true with regard to the secondary vortex deflecting the primary one and confining it to near the bubble. However, the secondary vortex is no longer weak and in fact has required a larger proportion of the kinetic energy from the source. As a result, and in contrast to the lower *Ma* case, the secondary vortex weakens the primary one in such a way that gravity has an adverse effect on the heat transfer.

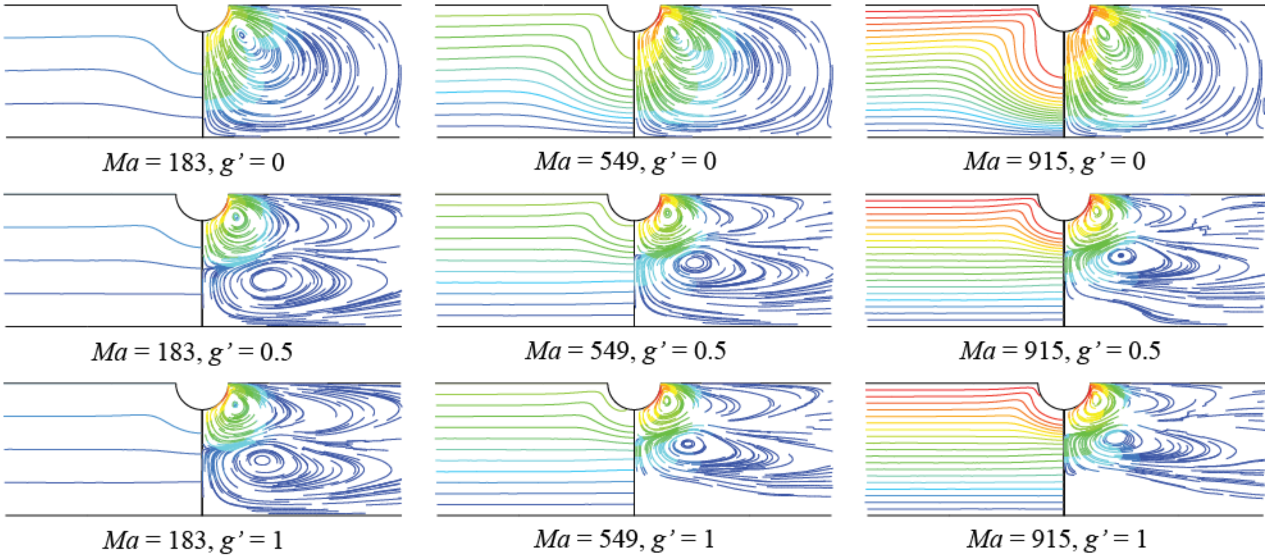

$Ma = 183$, $g' = 0$

$Ma = 549$, $g' = 0$

$Ma = 915$, $g' = 0$

$Ma = 183$, $g' = 0.5$

$Ma = 549$, $g' = 0.5$

$Ma = 915$, $g' = 0.5$

$Ma = 183$, $g' = 1$

$Ma = 549$, $g' = 1$

$Ma = 915$, $g' = 1$

Figure 12: Temperature contours and pathlines coloured by velocity for $Pr = 83$

5.4 Enhancement of heat transfer

The concept of an area of enhanced heat transfer surrounding the bubble has been introduced previously in [13, 22], and can be visualised in Figure 13. Previously it has been shown that under zero gravity conditions the area of improved heat transfer remains relatively constant, but this area notably changes in response to changing gravity levels.

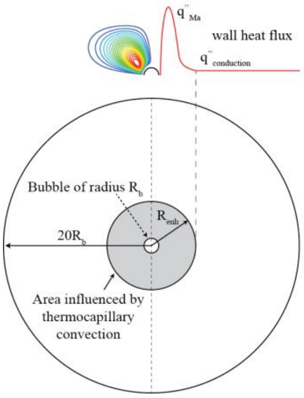

Figure 13: Area of enhanced heat transfer near bubble

Since the flow field is axisymmetric, the enhancement region is measured as a distance radially outward from the centre of the bubble. The criterion for defining enhancement is chosen to be a minimum 5% increase in local wall heat transfer compared to the conduction only case. The dimensionless enhancement radius is then calculated as

$$R_{enhancement} = \left.\frac{r}{R_b}\right|_{@1.05\, q''_{cond}} \qquad (21)$$

Figure 14 plots the enhancement radius versus dimensionless gravity level for a range of gravity levels. Interestingly, above a dimensionless gravity level of *g'* = 0.2, all curves converge. From this point the enhancement radius decreases slightly with increasing gravity level. This behaviour supports the theory that the flow structure is established at low gravity levels, and that increasing the gravity level further has minimal impact on heat transfer since the thermocapillary effect dominates in the region nearest the bubble where the majority of heat is transferred.

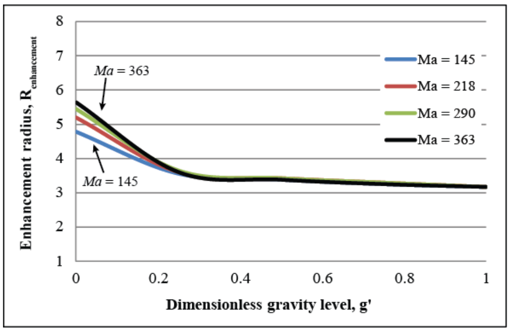

Figure 14: Enhancement radius vs. gravity level for $183 \le Ma \le 915$

Using the enhancement radius, an enhancement area can be defined which allows calculation of a hot wall Nusselt number. The enhancement radius will differ depending on the combination of *Ma*, *Ra* and *Pr*. To make a comparison between cases, the Nusselt number must be defined over the same area for all. Since the zero gravity case forms the baseline to which other cases are compared, an *effective radius* $R_{eff} = 6R_b$ is chosen (at terrestrial gravity an appropriate effective radius is $3R_b$). The hot wall effective area, $A_{eff\ hw}$, and Nusselt number for the hot wall, Nu_{hw}, are given by

$$A_{eff,hw} = \pi\left(R_{eff,hw}^2 - R_b^2\right) \qquad (22)$$

$$Nu_{hw} = \frac{\int_{R_b}^{R_{eff,hw}} q''_{Ma} 2\pi r dr}{\int_{R_b}^{R_{eff,hw}} q''_{cond} 2\pi r dr} \qquad (23)$$

Figure 15 plots the hot wall Nusselt number versus *Ma* using an effective radius of $6R_b$. The data from the Pr = 220, $145 \le Ma \le 363$ is graphed as solid dots in the figure. The trendlines are extended according to the results from the Pr = 83, $145 \le Ma \le 915$ numerical data. The figures show that more heat is transferred from the hot wall at zero gravity in almost all cases, and increasing the gravity level decreases the enhancement. These figures also imply that once gravitational forces are significant, increasing the Marangoni number will produce successively less profound increases in heat transfer, which is in agreement with the opinion that the buoyancy-driven vortex strips some of the mechanical energy from the thermocapillary roll.

To highlight the sensitivity of the Nusselt number to the choice of effective radius/area, Figure 16b plots the Nusselt number versus Marangoni number based on the effective radius at terrestrial gravity ($R_{eff} = 3R_b$). Using this effective area, the plot shows that in the region immediately surrounding the bubble, the interaction of the opposing thermocapillary and buoyancy forces actually results in increased heat transfer compared to zero gravity for low Marangoni numbers. The total amount of heat transferred is greater at 0-g however, since the absence of gravity allows the primary vortex to spread further into the channel and distribute the heat over a much larger area.

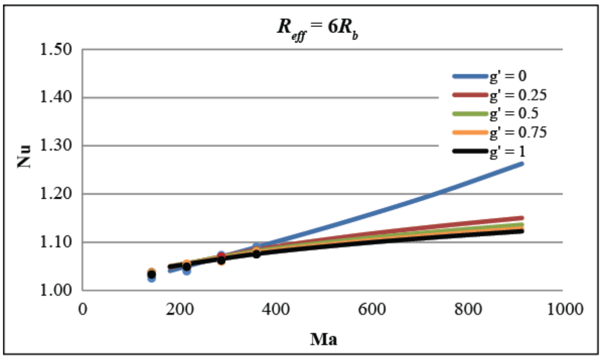

(a) Using $R_{eff} = 6R_b$

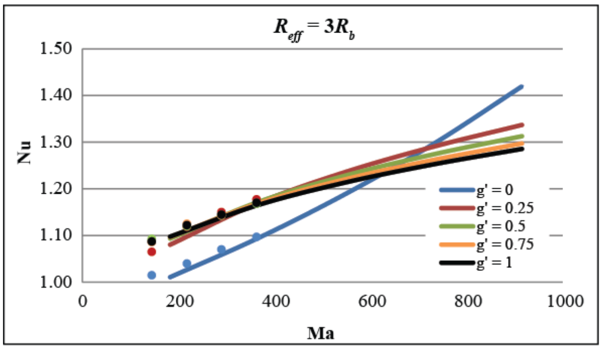

(b) Using $R_{eff} = 3R_b$

Figure 15: Nusselt number vs. Marangoni number using an effective radius of (a) $6R_b$ and (b) $3R_b$

Conclusions

Thermal Marangoni convection about a 1mm radius air bubble situated under a heated wall of constant temperature immersed in a silicone oil layer (Pr = 220) of constant depth 5mm was numerically investigated. Simulations were performed under steady state conditions for cases in which Marangoni and buoyancy forces opposed one another. The combined response to increasing Marangoni number and/or the magnitude of gravitational acceleration was investigated. For each Marangoni number simulated, primary thermocapillary-driven vortices were observed to develop on both sides of the bubble, along with a jet-like flow of liquid from the bubble tip that protruded into the bulk liquid below it. Beneath these primary flow structures, secondary buoyancy-driven vortices were observed to form from gravity levels as low as 0.1-*g*, and these slower-moving vortices rotated in opposite direction to the primaries. The wall heat flux profiles indicated that the interaction between the primary and secondary vortices resulted in greater peak heat fluxes, but overall the heat transferred was greater under zero gravity. Experimental validation of selected terrestrial gravity numerical results was obtained using PIV. For all experiments, steady-state Marangoni convection was observed. The experimental flow patterns showed good agreement with the numerical solutions.

Acknowledgements

The authors would like to acknowledge the Irish Research Council for Science and Engineering Technology (IRCSET) for their support in carrying out this research.

Nomenclature

Symbol	Description	Units
C_p	Sp. heat at constant pressure	J/kgK
g	gravitational acceleration	m/s^2
g^*	gravity level	-
H	cell height	m
k	thermal conductivity	W/mK
Ma	Marangoni number	-
p	pressure	Pa
p_{ref}	reference pressure	Pa
Pr	Prandtl number	-
q''	heat flux	W/m^2
Q	heat transferred	W
R_b	bubble radius	m
Re	Reynolds number	-
T_c	cold wall temperature	K
T_h	hot wall temperature	K
T_{ref}	reference temperature	K
v	velocity	m/s
v_{ref}	reference velocity	m/s
α	thermal diffusivity	m^2/s
β	thermal expansion coefficient	1/K
μ	dynamic viscosity	Pa.s
ν	kinematic viscosity	m^2/s
θ	dimensionless temperature	-
ρ	density	kg/m^3
σ	surface tension	N/m

References

[1] J. Straub, M. Zell, and B. Vogel, "What we learn from boiling under microgravity," *Microgravity Science and Technology*, vol. 6, pp. 239-247, 1993.

[2] J. Kim and J. F. Benton, "Highly subcooled pool boiling heat transfer at various gravity levels," *International Journal of Heat and Fluid Flow*, vol. 23, pp. 497-508, 2002.

[3] J. Straub, "The role of surface tension for two-phase heat and mass transfer in the absence of gravity," *Experimental Thermal and Fluid Science*, vol. 9, pp. 253-273, 1994.

[4] P. Arlabosse, L. Tadrist, H. Tadrist, and J. Pantaloni, "Experimental analysis of the heat transfer induced by thermocapillary convection around a bubble," *Transactions of the ASME. Journal of Heat Transfer*, vol. 122, pp. 66-73, 2000.

[5] S. Petrovic, T. Robinson, and R. L. Judd, "Marangoni heat transfer in subcooled nucleate pool boiling," *International Journal of Heat and Mass Transfer*, vol. 47, pp. 5115-5128, 2004.

[6] E. Koukan, G. Wozniak, K. Wozniak, and J. Siekmann, "Experimental study of flow fields around small gas bubbles under the combined

action of buoyancy and thermocapillarity," *Heat and Mass Transfer/Waerme- und Stoffuebertragung,* vol. 37, pp. 437-441, 2001.

[7] G. Wozniak, "Optical whole-field methods for thermo-convective flow analysis in microgravity," *Measurement Science & Technology,* vol. 10, pp. 878-85, 1999.

[8] G. Wozniak and K. Wozniak, "Buoyancy and thermocapillary flow analysis by the combined use of liquid crystals and PIV," *Experiments in Fluids,* vol. 17, pp. 141-6, 1994.

[9] K. Wozniak and G. Wozniak, "Temperature gradient driven flow experiments of two interacting bubbles on a hot wall," *Heat and Mass Transfer/Waerme- und Stoffuebertragung,* vol. 33, pp. 363-369, 1998.

[10] K. Wozniak, G. Wozniak, and T. Roesgen, "Particle-image-velocimetry applied to thermocapillary convection," *Experiments in Fluids,* vol. 10, pp. 12-16, 1990.

[11] J. Betz and J. Straub, "Numerical and experimental study of the heat transfer and fluid flow by thermocapillary convection around gas bubbles," *Heat and Mass Transfer/Waerme- und Stoffuebertragung,* vol. 37, pp. 215-227, 2001.

[12] M. Kassemi and N. Rashidnia, "Steady and oscillatory thermocapillary convection generated by a bubble," *Physics of Fluids,* vol. 12, pp. 3133-46, 2000.

[13] S. M. O'Shaughnessy and A. J. Robinson, "Numerical Investigation of Bubble Induced Marangoni Convection," *Interdisciplinary Transport Phenomena: Ann. N.Y. Acad. Sci,* vol. 1161, pp. 304-320, 2009.

[14] F. P. Pike, J. P.D. Miller, and J. K.O. Beatty, "Effect of Gas Evolution on Surface Boiling at Wire Coils," *Chemical Engineering Progress Symposium Series No. 17,* vol. 51, pp. 13-19, 1955.

[15] M. Barthes, C. Reynard, R. Santini, and L. Tadrist, "Non-condensable gas influence on the Marangoni convection during a single vapour bubble growth in a subcooled liquid," *Europhysics Letters,* vol. 77, p. 5 pp., 2007.

[16] B. K. Larkin, "Thermocapillary flow around hemispherical bubble," *AIChE Journal,* vol. 16, pp. 101-7, 1970.

[17] D. B. R. Kenning and Y. S. Kao, "Convective heat transfer to water containing bubbles: enhancement not dependent on thermocapillarity," *International Journal of Heat and Mass Transfer,* vol. 15, pp. 1709-17, 1972.

[18] R. Marek and J. Straub, "The origin of thermocapillary convection in subcooled nucleate pool boiling," *International Journal of Heat and Mass Transfer,* vol. 44, pp. 619-32, 2001.

[19] J. Straub, J. Betz, and R. Marek, "Enhancement of heat transfer by thermocapillary convection around bubbles-a numerical study," *Numerical Heat Transfer, Part A (Applications),* vol. 25, pp. 501-18, 1994.

[20] D. Raake, J. Siekmann, and C. H. Chun, "Temperature and velocity fields due to surface tension driven flow," *Experiments in Fluids,* vol. 7, pp. 164-172, 1989.

[21] S. M. O'Shaughnessy and A. J. Robinson, "Numerical investigation of bubble induced marangoni convection: Some aspects of bubble geometry," *Microgravity Science and Technology,* vol. 20, pp. 319-325, 2008.

[22] S. M. O'Shaughnessy and A. J. Robinson, "The Influence of the Magnitude of Gravitational Acceleration on the Marangoni Convection about an Isolated Bubble under a Heated Wall," *Heat Transfer Engineering,* vol. 30, pp. 1-13, 2009.

[23] P. Arlabosse, N. Lock, M. Medale, and M. Jaeger, "Numerical investigation of thermocapillary flow around a bubble," *Physics of Fluids,* vol. 11, pp. 18-29, 1999.

[24] C. Reynard, R. Santini, and L. Tadrist, "Experimental study of fluid-wall heat transfer induced by thermocapillary convection: influence of the Prandtl number," *Comptes Rendus de l'Academie des Sciences Serie II b/Mecanique,* vol. 331, pp. 237-44, 2003.

[25] C. Reynard, M. Barthes, R. Santini, and L. Tadrist, "Experimental study of the onset of the 3D oscillatory thermocapillary convection around a single air or vapor bubble.: Influence on heat transfer," *Experimental Thermal and Fluid Science,* vol. 29, pp. 783-793, 2005.

[26] C. D. Henry, J. Kim, and J. McQuillen, "Dissolved gas effects on thermocapillary convection during boiling in reduced gravity environments," *Heat and Mass Transfer,* vol. 42, pp. 919-23, 2006.

[27] J. U. Brackbill, D. B. Kothe, and C. Zemach, "A continuum method for modeling surface tension," *Journal of Computational Physics,* vol. 100, pp. 335-54, 1992.

[28] M. Raffel, C. Willert, S. Wereley, and J. Kompenhans, *Particle Image Velocimetry: A Practical Guide,* Second Edition ed. Berlin: Springer, 2007.

[29] A. Melling, "Tracer particles and seeding for particle image velocimetry," *Measurement Science & Technology,* vol. 8, pp. 1406-16, 1997.

[30] C. M. Tchen, "Mean value and correlation problems connected with the motion of small particles suspended in a turbulent fluid," PhD PhD Thesis, Delft University, Delft, 1947.

[31] C. Reynard, R. Santini, and L. Tadrist, "Experimental study of the gravity influence on the periodic thermocapillary convection around a bubble," *Experiments in Fluids,* vol. 31, pp. 440-446, 2001.

[32] C. Radulescu and A. J. Robinson, "The influence of gravity and confinement on Marangoni flow and heat transfer around a bubble in a cavity: a numerical study,"

Microgravity Science and Technology, vol. 20, pp. 253-9, 2008.

[33] C. Radulescu and A. J. Robinson, "Mixed convective heat transfer due to forced and thermocapillary flow around bubbles in a miniature channel: A 2D numerical study," *Heat Transfer Engineering,* vol. 31, pp. 335-343, 2010.

[34] C. Radulescu, "Mixed Thermocapillary and Forced Convection Heat Transfer Around a Hemispherical Bubble in a Miniature Channel—A 3D Numerical Study," *Heat Transfer Engineering,* vol. 33, pp. 596-608, 2012/05/01 2012.